Bulletin of the Seismological Society of America, Vol. 102, No. 2, pp. 773–782, April 2012, doi: 10.1785/0120110137

Ⓔ

Frequency-Dependent Seismic Attenuation within the Hispaniola Island Region of the Caribbean Sea

by D. McNamara, M. Meremonte, J. Z. Maharrey, S-L. Mildore, J. R. Altidore, D. Anglade, S. E. Hough, D. Given, H. Benz, L. Gee, and A. Frankel

Abstract We determine frequency-dependent attenuation $1/Q(f)$ for the Hispaniola region using direct *S* and *Lg* waves over five distinct passbands from 0.5 to 16 Hz. Data consist of 832 high-quality vertical and horizontal component waveforms recorded on short-period and broadband seismometers from the devastating 12 January 2010 **M** 7.0 Haiti earthquake and the rich sequence of aftershocks. For the distance range 250–700 km, we estimate an average frequency-dependent $Q(f) = 224(\pm 27)f^{0.64(\pm 0.073)}$ using horizontal components of motion and note that $Q(f)$ estimated with *Lg* at regional distances is very consistent across vertical and horizontal components. We also determine a $Q(f) = 142(\pm 21)f^{0.71(\pm 0.11)}$ for direct *S* waves at local distances, $\leq$100 km. The strong attenuation observed on both vertical and horizontal components of motion is consistent with expectations for a tectonically active region.

Online Material: Figures of filtered and broadband data, *Lg*- and *S*-wave amplitudes, and apparent frequency-dependent *Q*, and tables of earthquake and station parameters.

Introduction

In this study we focus on the attenuation characteristics of the Caribbean island of Hispaniola and the surrounding region, ranging from Jamaica and Cuba in the west to Puerto Rico in the east (Fig. 1). The island of Hispaniola, which comprises the countries of Haiti and the Dominican Republic, is mountainous with maximum elevations of nearly 4000 m and lies at the complex boundary between the North American and Caribbean tectonic plates (Fig. 1). Relative plate motion is approximately 20 m/yr with Hispaniola at the transition zone between a subduction zone to the east (Fig 1, Puerto Rico trench) and a dominantly strike-slip plate boundary to the west (Fig. 1, Cayman trench) (Bird, 2003; Manaker *et al.*, 2008). Two major crustal transpressional strike-slip fault systems—the Septentrional fault to the north and the Enriquillo Plantain Garden fault to the south (Manaker *et al.*, 2008; Calais, *et al.*, 2010)—run roughly east–west across Hispaniola, posing a significant earthquake hazard (Prentice, *et al.*, 2010; Frankel *et al.*, 2010; Mann *et al.*, 2002). On 12 January 2010, an M_w 7.0 earthquake occurred in this region killing more than 230,000 people in the city of Port-au-Prince, Haiti, and causing submarine landslides that resulted in the production of local tsunami inundation (Hornbach *et al.*, 2010). The earthquake was the largest to strike the southern part of Hispaniola since 3 June 1770 (Calais *et al.*, 2010) and was due to a complex rupture process involving slip on multiple faults (Hayes *et al.*, 2010). In the year following the **M** 7.0 earthquake, numerous aftershocks have occurred with a diffuse distribution of hypocenters that are located primarily at the western margin of the region of significant slip, suggesting that most of these events reflect triggered slip on minor faults rather than defining the mainshock coseismic rupture zone (Hayes *et al.*, 2010).

Historically, only a small number of recordings of moderate-to-large–magnitude earthquakes (**M** > 5) at local distances were available in the Hispaniola region, limiting the determination of ground-motion relations for magnitudes and distances for engineering interest. In this study, we utilize the Haiti **M** 7.0 mainshock and a rich sequence of aftershocks to solve for frequency-dependent attenuation $Q(f)$ using the seismic phases *Lg* at regional distances and direct *S* waves at local distances. $Q(f)$ is an important physical parameter and is required for successful simulation of strong ground motion using techniques such as semiempirical modeling (Joshi and Midorikawa, 2004), composite source modeling (Zeng *et al.*, 1994), and stochastic simulation (Boore, 1983).

The *Lg* phase propagates with a group velocity of about 3.5 km/s, the average crustal shear-wave velocity, and is commonly observed as the dominant phase on high-frequency seismograms at regional distances (e.g., Isacks and Stephens,

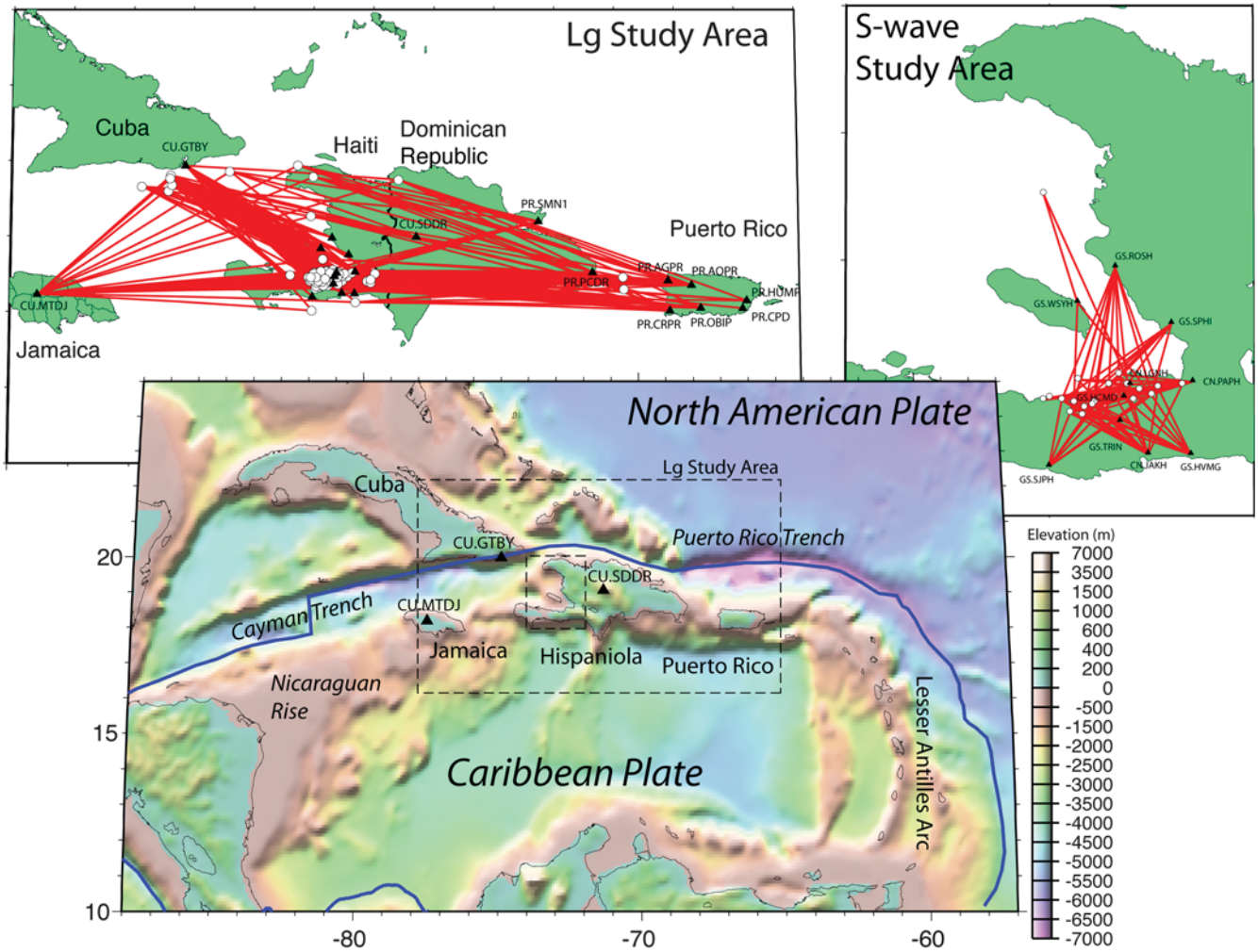

Figure 1. Tectonic setting and study area maps showing the tectonic plate boundary (blue lines) between the North American and Caribbean plates (Bird, 2003). The small inset boxes (dashed lines) are the *Lg* and *S*-wave *Q* study areas. The *Lg* study area has 749 *Lg* propagation paths (red lines) from 125 shallow ($h \leq 15$ km) earthquakes (white circles) (Ⓔ see Table S1, available in the electronic supplement to this paper) recorded at 25 short-period and broadband seismic stations (black triangles) (Ⓔ see Table S2, available in the electronic supplement to this paper). The *S*-wave study area shows 90 *S*-wave propagation paths (red lines) from 22 shallow ($h \leq 15$ km) earthquakes (white circles) (Ⓔ see Table S1, available in the electronic supplement to this paper) recorded at 10 short-period and broadband seismic stations (black triangles) (Ⓔ see Table S2, available in the electronic supplement to this paper).

1975; McNamara and Walter, 2001). *Lg* is generated by a superposition of higher-mode surface waves (Oliver and Ewing, 1957; Knopoff *et al.*, 1973) or as multiply-reflected shear energy in a crustal waveguide (Press and Ewing, 1952; Gutenberg, 1955). Consequently, *Lg* provides a good measure of path-averaged crustal properties such as shear-wave velocity and attenuation. *Lg* amplitude is sensitive to lateral heterogeneity in the crust due to varying tectonic environments (Erickson, *et al.*, 2004). *Lg* attenuation is higher for tectonically active regions than for stable continental interiors (Frankel *et al.*, 1990; Atkinson *et al.*, 1992; Xie and Mitchell, 1993; McNamara *et al.*, 1996; Benz *et al.*, 1997; McNamara, 2000; Ottemoller, 2002). Several mechanisms have been proposed to explain these observations: differences in crustal heterogeneity leading to differences in absorption of high-frequency energy (Aki, 1980), differences in crustal temperature (Frankel *et al.*, 1990), and variations in crustal structures that control elastic wave propagation (Gregersen, 1984; Kennett, 1986). *Lg* is generally observed to propagate inefficiently or to be completely absent in thin oceanic crust (Kennett, 1986; McNamara *et al.*, 2001; Zhang and Lay, 1995).

Numerous researchers have estimated $Q(f)$ for the Earth's crust throughout the world (Aki, 1980; Chavez and Priestly, 1986; Frankel *et al.*, 1990; Atkinson and Mereu, 1992; McNamara *et al.*, 1996; Benz *et al.*, 1997). The frequency-dependent quality factor $Q(f)$ is commonly modeled using a power law of the form

$$Q(f) = Q_0(f/f_0)^{\eta}, \tag{1}$$

where f_0 is a reference frequency (generally 1 Hz), Q_0 is Q at the reference frequency, and η is assumed to be constant over the frequencies of interest. In this study we use data

from broadband instruments to determine $Q(f)$ in the Hispaniola region and compare the results with attenuation determined for other regions.

Q Inversion Methods

Data Selection and Amplitude Measurement

Lg and *S*-wave amplitudes used in the inversion were restricted to stations that recorded at least two earthquakes and earthquakes recorded by at least two stations. In addition to visual inspection, we required a signal-to-noise root mean square (RMS) amplitude ratio greater than two, where the noise amplitude is taken from the *P* coda rather than preceding the *P* wave. This step eliminated very few paths, because *Lg* is generally the dominant arrival on regional seismograms, and ensured observations where *Lg* is present at all distances. The goal was to eliminate paths crossing *Lg*-blocking structures, such as abrupt crustal thickness transitions from continental to oceanic crust, that would bias the regional Q estimate (McNamara and Walter, 2001). The RMS amplitude for *Lg* was windowed from 3.6 to 3.0 km/s, direct *S* from 4.8 to 3.6 km/s and the *P* coda was windowed from 5.8 to 4.8 km/s. The window for the *P* coda was chosen to select the scattered energy between faster crustal *P* waves (*Pg*) and slower upper mantle *S* waves (*Sn*). Regional and local waveforms that passed the signal-to-noise criteria were further processed to obtain *Lg* and direct *S*-wave spectral amplitude measurements. This included deconvolution of the instrument response transfer function from the band-pass-filtered seismogram. Finally, the RMS amplitude of *Lg* and *S* were measured in five one-octave passbands with center frequencies of 0.75, 1.5, 3, 6 and 12 Hz. After applying the earthquake and waveform selection criteria to over 2000 regional seismograms, nearly 850 high-quality *Lg* and *S*-wave waveforms remained: from 125 events recorded at 25 stations. Figure 2 shows an example of well-recorded *S*-wave and *Lg* arrivals that passed the data selection criteria for an earthquake (20 March 2010, 18 h 8 m 8.72 s) located off the southeastern shore of Cuba (19.67 N, 75.33 W; 14 km depth; and M_w 5.6) (Ⓔ Table S1, available in the electronic supplement to this paper) recorded at the portable aftershock station GS.WSYH.00.EHE ($\Delta = 275.4$ km) (Fig. 1b and Ⓔ Table S2, available in the electronic supplement to this paper). Seismic velocity windows and phases are labeled in Figure 2 at the five filtered passbands used in this study. In general, *S*-wave and *Lg* amplitudes decrease with increasing frequency content. We also observe measureable *Lg* amplitudes (Fig. 2) despite significant oceanic paths (Fig. 1; McNamara and Walter, 2001). Ⓔ Additional filtered seismograms are available as an electronic supplement to this paper (Fig. S1).

Single Frequency Q Inversion

The inversion method used in this study to estimate $Q(f)$ is well known (Frankel *et al.*, 1990; McNamara *et al.*, 1996; McNamara, 2000; Erickson *et al.*, 2004) and described in detail by Benz *et al.* (1997). The observed amplitude A at frequency f for the jth earthquake recorded at the ith station can be modeled as

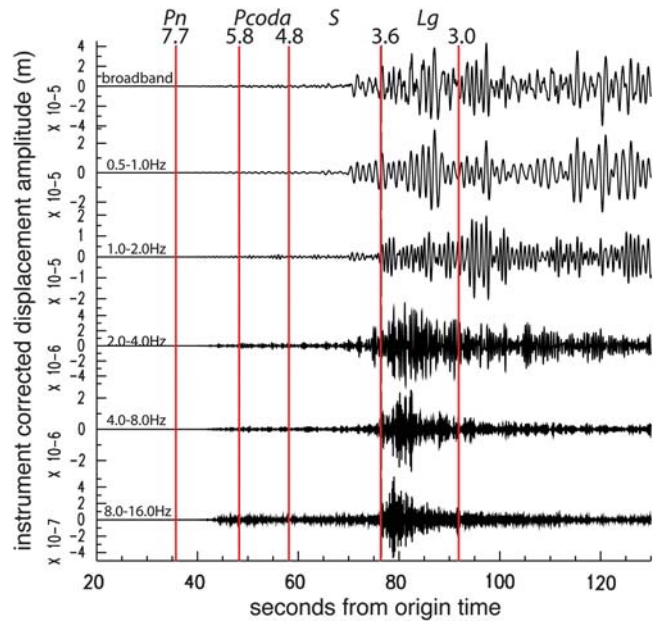

Figure 2. The 20 March 2010, 18 h 8 m 8.72 s earthquake located off the southeastern shore of Cuba (19.67 N, 75.33 W; 14 km depth; and M_w 5.6) recorded at the portable aftershock station GS.WSYH ($\Delta = 275.4$ km). Shown is the GS.WSYH.00.EHE (100 samples per second) component of the instrument corrected displacement seismogram. The seismogram is filtered in five passbands. Seismic velocity windows (red lines) and phases used in the data selection procedure are shown.

$$A_{ij}(f) = R_{ij}^{-\gamma} S_j(f) G_i(f) e^{-\pi f R_{ij}/Q\beta}, \tag{2}$$

where $S_j(f)$ is the source spectrum, $G_i(f)$ is the site amplification, R_{ij} is the epicentral distance between the earthquake j and station i, γ is the exponent for geometrical spreading, Q is the quality factor at frequency f, and β is the average shear-wave velocity for the crust—3.5 km/s for this study. Taking the logarithm of equation (2) yields the following:

$$\ln A_{ij}(f) + \gamma \ln R_{ij} = \ln G_i(f) + \ln S_j(f) - \pi f R_{ij}/Q\beta. \tag{3}$$

When amplitude corrected for geometric spreading (the left side of equation 3) is plotted with respect to distance, the right side of equation (3) describes a line where the receiver (G_i) and source (S_j) terms control the intercept, and the Q term controls the slope. Using a dataset with many source–receiver pairs, a system of linear equations can be set up based on equation (3). The system of equations can be expressed as

$$\boldsymbol{Ax} = \boldsymbol{t}, \tag{4}$$

where $\boldsymbol{A}$ is the system matrix made up of the parameter coefficients of equation (3), $\boldsymbol{x}$ is a column vector containing the

unknown source (S) and receiver (G) terms and the regional Q term, and the $\boldsymbol{t}$ vector is comprised of the left hand side of equation (3). The system matrix $\boldsymbol{A}$ is made up of mostly ones and zeros, with the last column listing a portion of the last term of equation (3), $(\frac{-\pi f R_{ij}}{\beta})$. We solve for each frequency independently, and the known variables are R, f, and β for each source–receiver pair. A singular value decomposition (SVD) inversion algorithm is then applied to solve for the unknown variables S_j and G_i, as well as a regionally averaged Q for a single frequency passband with center frequency f (e.g., Menke, 1980; Aster *et al.*, 2002).

Sensitivity of $Q(f)$ to Geometric Spreading

In developing attenuation models, we must determine if $Q(f)$ can be determined by assuming a single geometric spreading rate γ or if an epicentral distance dependence is indicated. Several previous studies have described the geometrical spreading function as a hinged-trilinear functional form, in which amplitude decay varies as a function of epicentral distance (Atkinson and Mereu, 1992; Atkinson and Boore, 1995). For example, Atkinson (2004) describes attenuation in eastern North America by parameterizing geometrical spreading as $R^{-1.3}$ to 70 km, as $R^{0.2}$ for 70–130 km, and $R^{-0.5}$ beyond 130 km. This parameterization is interpreted as reflecting changes in the dominant wave type. At close distances, the direct S waves dominate and the attenuation rate is steep, $R^{-1.3}$. At distances beyond 70 km, the postcritical reflections from the Moho discontinuity join the direct S waves, increasing energy levels and decreasing the attenuation rate, $R^{0.2}$. At regional distances, multiple refractions and reflections of the shear waves trapped in the crustal waveguide Lg dominate seismic records, and the attenuation rate changes to the commonly used form $R^{-0.5}$ (Frankel, 1991; McNamara *et al.*, 1996; Benz *et al.*, 1997). In an attenuation study in Puerto Rico, Motazedian and Atkinson (2005) found significant distance-dependent geometrical spreading and adopted a hinged-trilinear functional form specific to Puerto Rico, where geometrical spreading is described by R^{-1}, R^{0}, and $R^{-0.5}$, with hinge points at 75 and 100 km.

Figure 3 shows the distribution of raw horizontal component (BHE, BH1) Lg- and S-wave amplitudes, measured in the 1–2 Hz frequency band as a function of distance. S-wave (green squares) and Lg (green circles) amplitudes for the **M** 7.0 Haiti earthquake (12 January 2010, 21 h 53 m 10 s), recorded only at permanent stations, and an **M** 4.2 (28 March 2010, 07 h 16 m 17 s), recorded by nearly all stations in the study, are also shown. We observe a significant amount of scatter. Amplitude variability is due to the range of magnitudes spanned by the dataset, variability in regional Q, site amplification, and possible errors in the instrument response transfer function. Earthquake magnitude variation will be absorbed into the source term (S) in equation (3), and any systematic amplitude contributions due to site response amplification and/or instrument response will be absorbed into the receiver term (G). Because we cannot separate site amplification from instrument response contributions, we are not able to interpret the receiver (G) term as being due to regional site amplification variations.

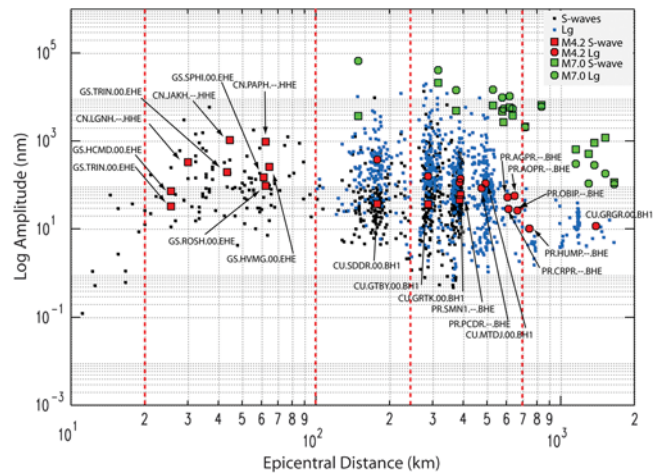

Figure 3. Raw 1–2 Hz horizontal component local S-wave (black squares) and regional Lg (blue squares) amplitudes from stations BHE and BH1 plotted as a function of distance. Also plotted are S-wave (green squares) and Lg (green circles) amplitudes for the **M** 7.0 Haiti earthquake (12 January 2010, 21 h 53 m 10 s) recorded by permanent stations in the region and S-wave (red squares) and Lg (red circles) amplitudes for an M 4.2 earthquake (28 March 2010, 07 h 16 m 17 s) recorded by both portable and permanent stations (Fig. 1a, b; Ⓔ see Table S2, available in the electronic supplement to this paper) in the study. Changes in slope at distances of 20, 250, and 700 km indicate changes in attenuation as a function of epicentral distance.

Both phase type and attenuation rate changes as a function of epicentral distance are clearly observed in Figure 3. In general, Lg is not well established and separate from crustal S waves in paths shorter than 100 km. At distances <100 km, crustal S waves are the largest phase on the seismogram (Fig. 3, black squares). At distances from 100 to 250 km, Lg develops (Fig. 3, blue squares) while crustal S waves are still present. Beyond 250 km, body waves consist of small amplitude mantle head waves (Sn), and crustal Lg dominates the seismogram. Despite the scatter in Figure 3, we observe that the attenuation rate depends strongly on epicentral distance, with clear changes in slope at several hinge points. Observed raw amplitudes show significant changes in slope at distances of 20 km, 250 km, and 700 km (Fig. 3). This observation is consistent with observations made previously in other regions (Atkinson, 2004; Motazedian and Atkinson, 2005), although the hinge points in our dataset are unique to the crustal attenuation and velocity structure of the Hispaniola region.

P-Wave Velocity Structure

We analyzed the travel times of first arriving P waves in order to further investigate crust and upper mantle structure deduced from the distance-dependent Lg and S-wave amplitudes observed in Figure 3. This dataset yielded over 2000 travel times, which were assigned a quality factor from A to

D, depending on the precision and confidence in the phase pick. Figure 4 shows the A and B quality travel times versus distance for 503 first arriving *P* waves plotted with a reducing velocity of 7.7 km/s. Clear changes in slope are observed at 200 km (Fig. 4, Xd) and 700 km (Fig. 4, Xm), suggesting that three separate *P* phases are present in the dataset. A least-squares fit to travel times at distances up to 200 km results in a propagation velocity of 6.6 km/s and is most consistent with the crustal *Pg* phase. Travel times at distances of 200–700 km propagate at 7.7 km/s and are most consistent with the mantle head wave (*Pn*) while travel times at epicentral distances >700 km propagate at 8.3 km/s and are likely due to *P* waves that propagate at greater depths in the mantle (Fig. 4).

The crossover distance (Xd = 200 km) and intercept time ($Ti = 2.97$ s) determined from the least-squares fit to the mantle head-wave *Pn* (Fig. 4) can be used to uniquely determine crustal thickness from standard refraction seismology methods (Dobrin and Savit, 1988). Intercept time (*Ti*) is expressed by the following:

$$Ti = 2h\sqrt{\frac{1}{V_{Pg}^2} - \frac{1}{V_{Pn}^2}}, \tag{5}$$

where h is crustal thickness, V_{Pg} is crustal *Pg* velocity, and V_{Pn} is mantle *Pn* velocity. Using the values from Figure 4, we compute a crustal thickness of 20.6 km. This result is consistent with receiver function results obtained from the Earthscope Automated Receiver Survey (EARS) at the Incorporated Research Institutions in Seismology (IRIS) Data Management Center (DMC) for the USGS Global Seismographic Network (GSN) station CU.SDDR (Fig. 1a; Ⓔ Table S1, available in the electronic supplement to this paper) in the Dominican Republic after the methods of Crotwell and Owens (2005), which suggest a crustal thickness of 20 km and crustal velocity of 6.6 km/s. Our observed average crustal *Pg* velocity of 6.6 km/s is quite fast for a tectonic region,

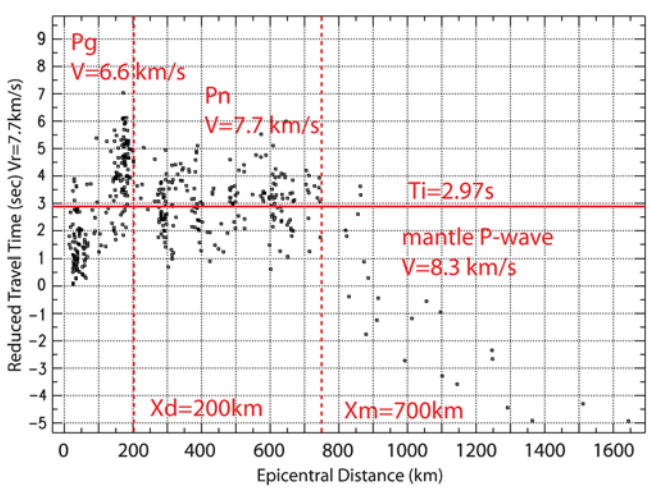

Figure 4. First arriving *P*-wave travel times plotted with a reducing velocity of 7.7 km/s.

and the crustal thickness of 20 km is very thick for an oceanic environment. The crust in this region, from eastern Cuba to eastern Puerto Rico (Fig. 1), is made up of both exposed islands and shallow ocean depths. Thickened island arc oceanic crust, due to active collision tectonics along the north plate boundary (Mann *et al.*, 2002), is consistent with our observations of fast *P*-wave velocity and thick oceanic crust, as well as shallow bathymetry.

The crustal structure determined from local and regional distance first arriving *P* waves is roughly consistent with the path-length dependent *S*-wave and *Lg* amplitudes observed in Figure 3. At distances <100 km, crustal waves (*Pg* and *Sg*) dominate the seismogram. At distances from 100 to 250 km, *Lg* develops while both crustal *P* and *S* waves are still present. Beyond 200–250 km, body waves consist of small amplitude mantle head waves (*Pn* and *Sn*) and crustal *Lg* dominate the seismogram. Based on these observations, we invert separately for $Q(f)$ using direct *S* waves at distances <100 km, assuming R^{-1}, and *Lg* at distances of 250–700 km, assuming $R^{-0.5}$. The hinge point positions for Haiti and the Hispaniola region are unique. However, we use geometric spreading functions consistent with those of previous studies in the region (Atkinson, 2004; Motazedian and Atkinson, 2005).

Results

Lg Q Results

Vertical component *Lg* amplitudes, measured in five frequency bands and corrected for the source (S_j), and receiver (G_i) terms are shown in Figure 5. The straight lines represent the best fitting *Q* for the particular frequency band from equation 3. In each frequency band the inversion procedure solves for an average *Q* using 749 high-quality *Lg* amplitude observations from 126 events recorded at 25 stations with a distance range of 250–700 km (Fig. 5). Ⓔ Horizontal component *Lg* amplitudes, measured in five frequency bands and corrected for the source (S_j), and receiver (G_i) terms are available as an electronic supplement to this paper (see Figs. S2 and S3).

S-Wave *Q* Results

Ⓔ Horizontal component *S*-wave amplitudes, measured in five frequency bands and corrected for the source (S_j), and receiver (G_i) terms are available as an electronic supplement to this paper in Figure S4. The straight lines represent the best fitting *Q* for the particular frequency band from equation 3. In each frequency band, the inversion procedure solves for an average *Q* using 90 high-quality *S*-wave amplitude observations from 22 events recorded at 11 stations with a distance range of 25–80 km (Ⓔ see Fig. S4, available in the electronic supplement to this paper).

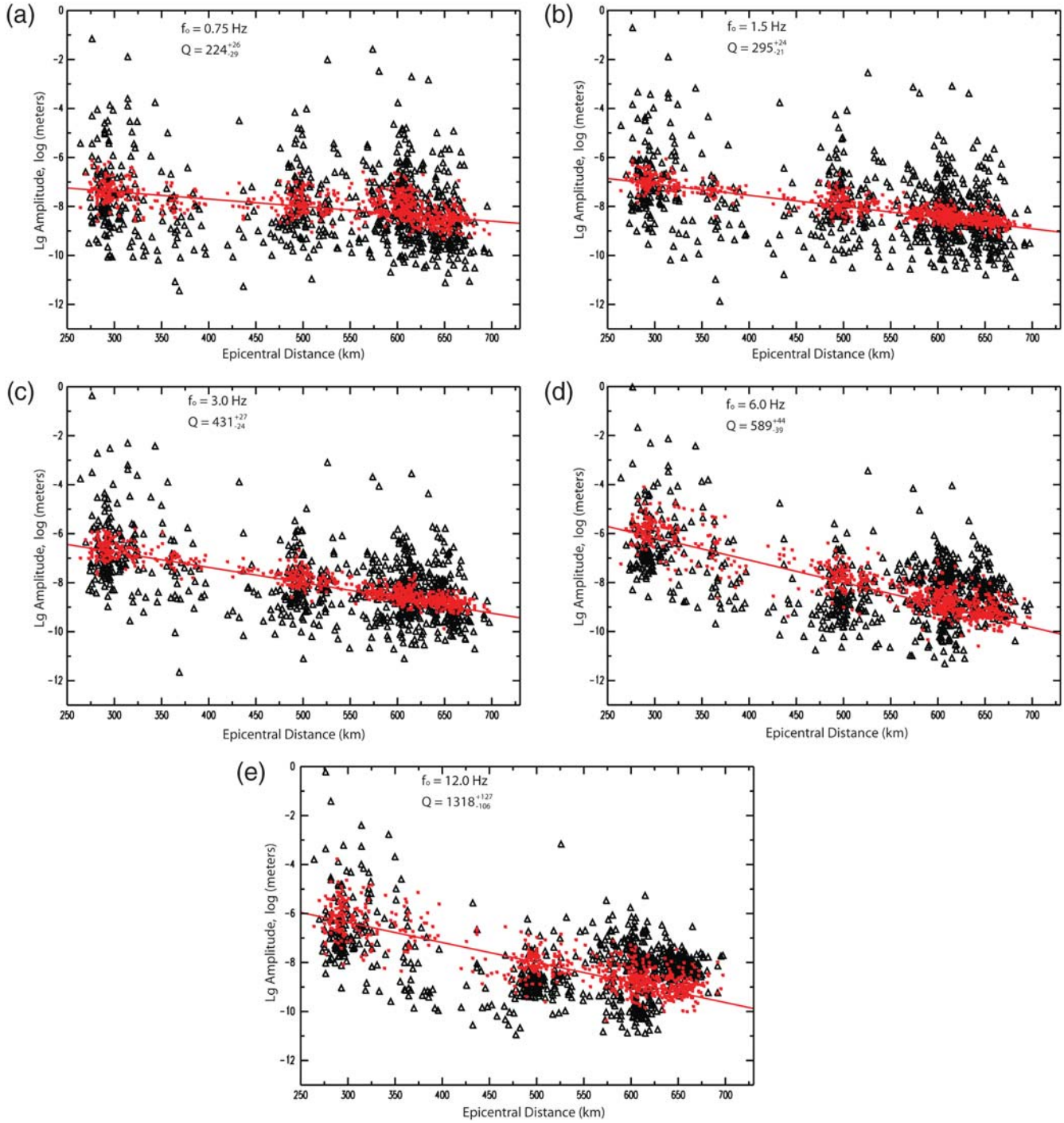

Figure 5. Original vertical component (stations SHZ, HHZ, and BHZ) *Lg* amplitudes (black triangles) corrected for source and receiver terms determined in the *Q* inversion (red squares) (a) 0.75 Hz *Lg Q* results. (b) 1.5 Hz *Lg Q* results. (c) 3.0 Hz *Lg Q* results. (d) 6.0 Hz *Lg Q* results. (e) 12.0 Hz *Lg Q* results using vertical components.

$Q(f)$ Results

By repeating the inversion over five octaves, with center frequencies of 0.75, 1.5, 3, 6, and 12 Hz, we obtain a Q estimate for each passband. A weighted *L1* norm least-squares regression analysis is then used to fit the frequency-dependent Q function $Q(f)$, equation (1), to the Q estimates. Taking the logarithm of both sides of equation (1) yields

$$\ln Q = \ln Q_0 + \eta \ln(f) - \eta \ln(f_0), \tag{7}$$

where Q_0 and η are the unknowns to be determined.

We find *Lg*, $Q(f) = 245(\pm 31) f^{0.61(\pm 0.082)}$, for the vertical components of motion (Ⓔ see Fig. S5, available in the electronic supplement to this paper) and for the horizontal components of motion in the east–west direction (BHE, HHE, SHE, and BH1), $Q(f) = 228(\pm 27) f^{0.65(\pm 0.081)}$ (Ⓔ

see Fig. S6, available in the electronic supplement to this paper), and in the north–south direction (BHN, HHN, SHN, and BH2), $Q(f) = 220(\pm 21)f^{0.62(\pm 0.064)}$ (Ⓔ see Fig. S7, available in the electronic supplement to this paper). Finally, we combine all horizontal components and determine an average $Q(f) = 224(\pm 27)f^{0.64(\pm 0.073)}$, which is the final *Lg* $Q(f)$ model presented in this analysis. We observe that *Lg* $Q(f)$ estimated at regional distances is very consistent across vertical and horizontal components. It is interesting to note that the simple SVD linear model fits *Lg* Q values in the mid-frequencies, however at both low and high frequencies, Q values are generally higher than that of the model, suggesting that η steepens with increasing frequency (Fig. 6; Ⓔ see Figs. S6 and S7, available in the electronic supplement to this paper). This has also been observed in previous studies in the continental United States (Erickson *et al.*, 2004) and suggests that more complex modeling may be required. In addition to *Lg* $Q(f)$, we find $Q(f) = 142(\pm 21)f^{0.71(\pm 0.11)}$ using only horizontal component direct *S* waves at local distances ≤100 km (Ⓔ see Fig. S8, available in the electronic supplement to this paper). For comparison, $Q(f)$ results for all *Lg* components and the direct *S* wave are shown in Figure 7.

Error and Resolution

We examined the mean and standard deviation of Q for each region for all frequencies by resampling the original dataset using the delete-j jackknife resampling technique modeled after the method of Efron and Tibshirani (1993). To achieve consistency for the jackknife estimate of standard deviation, we left out at least $d = \sqrt{n}$, where n is the total number of observations and d is the number of observations removed from the complete dataset. To obtain an error bound, we removed d number of randomly selected observations

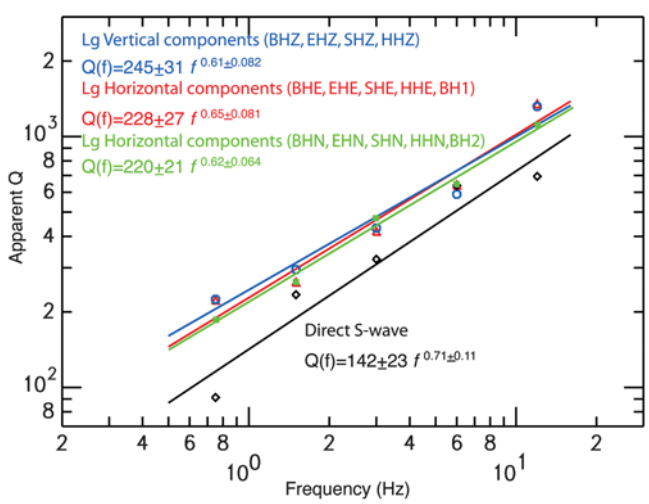

Figure 6. Frequency-dependent *Lg* $Q(f)$ for vertical components of motion (red) $Q(f) = 245(\pm 31)f^{0.61(+0.082)}$ and horizontal components of motion (blue; stations BHE, HHE, SHE, and BH1) $Q(f) = 228(\pm 27)f^{0.65(\pm 0.081)}$ (green; stations BHN, HHN, SHN, and BH2) $Q(f) = 220(\pm 21)f^{0.62(\pm 0.064))}$. Also shown is the direct *S*-wave (black) $Q(f) = 142(\pm 21)f^{0.71(\pm 0.11)}$.

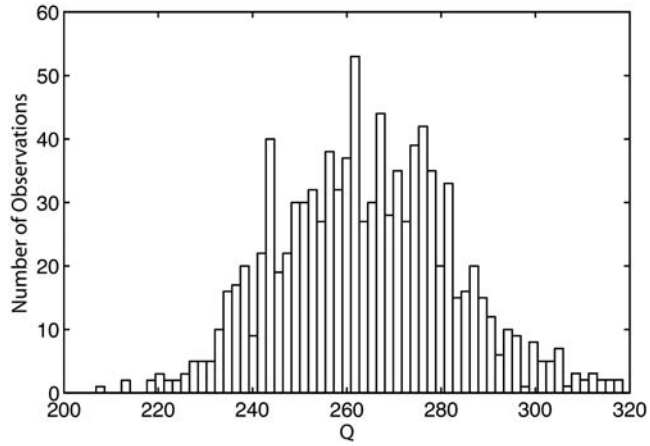

Figure 7. Histogram of 1000 jackknife Q inversions for horizontal component *Lg* amplitudes at 1.5 Hz. In this example, the total number of observations (n) = 742 and the number of observations removed for each jackknife inversion (d) = 148 are shown. Note the normal distribution of Q values. From 1000 randomly sampled datasets, the average jackknife Q value is 264.25 ± 19.78.

from the total n number of observations to create 1000 new jackknife datasets, and then inverted each jackknife dataset to determine 1000 Q values. From these 1000 Q values, we calculate a standard deviation (2σ) and a mean value for the region at a desired frequency. We then compared the mean Q from the 1000 jackknife datasets to the Q computed from the entire dataset to test for stability and accuracy.

Figure 7 shows a histogram of the results obtained from 1000 different inversions of randomly selected jackknife datasets using the horizontal (SHE, HHE, BHE, and BH1) *Lg* amplitudes measured in the 0.5–1.0 Hz band (center frequency = 1.5 Hz). We randomly removed 20% of the observations from the complete dataset ($n = 742$) to create 1000 new jackknife datasets, and then inverted each new reduced dataset to obtain 1000 Q values. The mean and standard deviation were calculated from this set of 1000 Q values to establish error estimates for the region. In this example, Q computed from the complete dataset is 262.56 (Ⓔ see Fig. S2b in the electronic supplement to this paper). After 1000 randomly sampled datasets, with a 20% reduction in the number of data points, the average jackknife Q value is 264.25 ± 19.78, a difference of only 1.75 from the Q determined from the complete dataset.

We also tested the stability of our datasets by removing an increasing number of waveforms to determine at which point the inversion becomes unstable, and Q is no longer well resolved. Our results remain stable, with a standard deviation less than 50 and a delta Q less than 50, until about 75% of the data are removed (Fig. 8). This suggests that Q can be determined with relatively few observations and that adding more observations merely decreases the error. Since the variation of Q from the different datasets likely represents the regional variability of the Q structure, these observations reinforce our confidence that our Q results are stable estimates of the frequency-dependent regional average attenuation structure.

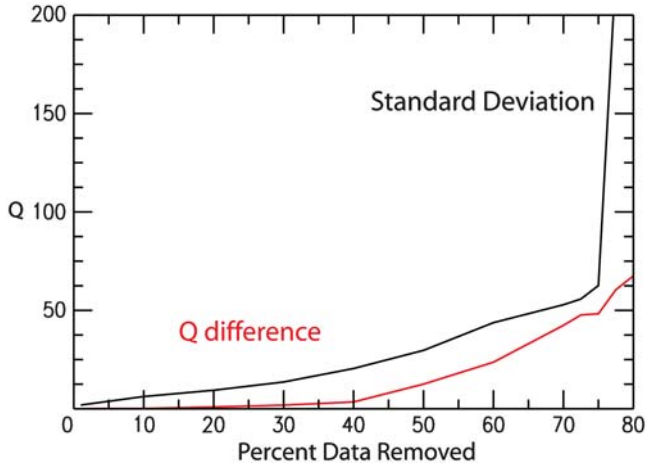

Figure 8. In this plot we show the difference between the average Q determined from 1000 jackknife datasets and the Q inverted from the original complete dataset (red line) versus the percent of data removed. Data are the same as used in Figure 8. Note that the Q difference is very low until 40% of the data are removed. The Q difference gradually increases as an increasing percentage of data are removed. The black line is the standard deviation of the jackknifed Q result versus the percent of data removed from the original dataset before inversion. Note the standard deviation gradually increases until about 75 percent of the original data are removed.

Discussion

Our results show that the attenuation properties of *Lg* differ from those of the direct *S* wave in Hispaniola. Differences reflect a depth dependence of attenuation: the *Lg* waveform samples the entire crust, including the deeper crust, which is likely to be characterized by lower attenuation (higher Q; Hough and Anderson, 1988), while the direct *S* waves are more strongly controlled by the upper crust.

Both direct *S* and *Lg* $Q(f)$ results for Hispaniola can be compared with results determined for other regions. Of the regions for which *Lg* attenuation has been investigated, the regional *Lg* $Q(f)$ results from this study are most similar to the Basin and Range and south-central Alaska (McNamara, 2000; Erickson *et al.*, 2004). The direct *S*-wave $Q(f)$ estimated in this study is most similar to previous results from southern California. In addition, Raoof *et al.* (1999) found $Q(f) = 180f^{0.45}$ for southern California using local *S* waves, and Frankel *et al.* (1990) computed $Q = 110$ at 3 Hz for southern California, using a geometric spreading function of R^{-1}. The local attenuation properties of Hispaniola, computed in this study, are thus consistent with values estimated for other tectonically active regions.

The nearest region to our study is Puerto Rico (Fig. 9), for which Motazedian and Atkinson (2005) estimate $Q(f) = 359f^{0.59}$ using earthquakes as deep as 200 km. The frequency dependence of our results and Puerto Rico are similar; however Q_0 is lower in our study. The difference between Q_0 in Puerto Rico and in the Hispaniola region might reflect several factors including regional variability in attenuation and the selection of only shallow crustal earthquakes in this study.

Despite the large number of ocean paths traversing the Caribbean Sea surrounding the island of Hispaniola, *Lg* is generally observed to propagate efficiently and is well observed on seismograms. It is interesting to note that while our observed *Lg* $Q(f)$ is relatively low and indicative of an active tectonic region, *Lg* amplitudes are significantly higher than might be expected in an oceanic environment (Zhang and Lay, 1995; McNamara and Walter, 2001). For the Hispaniola region of the Caribbean Sea considered in this study (Fig. 1), the *Lg* wave train is well developed, suggesting the presence of continental crust. However, *Lg* paths in this study traverse areas of shallow ocean bathymetry associated with thickened ocean arc crust at the active boundary between the North American and Caribbean tectonic plates (Fig. 1), as opposed to thin oceanic crust, which is typically associated with deeper bathymetry (for a more detailed map of the region see Tarr *et al.*, 2010). In addition to the quantitative $Q(f)$ results presented here, we note that *Lg* propagation is not exclusive to continental regions but can also propagate in thickened oceanic crust. Because of the complex nature of the crust, we expect that Q will be highly variable throughout other parts of the Caribbean region. Future work will consider Q and *Lg* propagation for the broader region using previously established tomographic methods (McNamara and Walter, 2001; Pasyanos *et al.*, 2009).

Computing region-specific $Q(f)$ is important to simulating the strong ground shaking for large earthquake scenarios for hazard mitigation planning and for the improvement of probabilistic assessments of seismic hazard, such as the USGS national seismic hazard maps that are used for seismic provisions in building codes (Frankel *et al.*, 2000; Frankel *et al.*, 2002; Petersen *et al.*, 2008). Attenuation characteristics are also important for magnitude detection threshold models computed to optimize seismic network design for earthquake

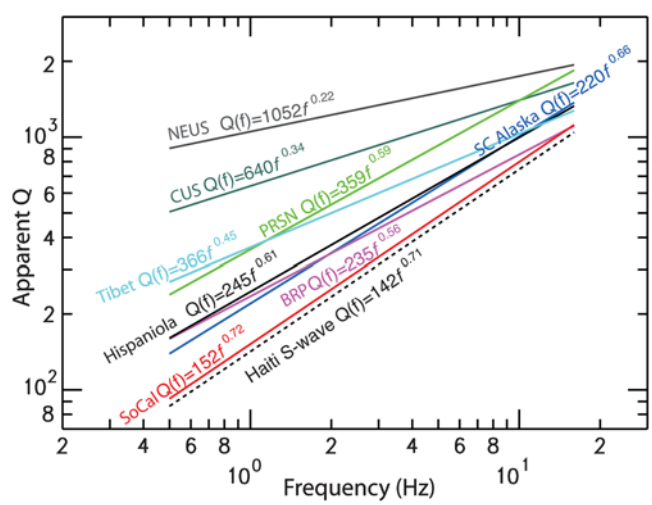

Figure 9. $Q(f)$ results from this study compared to results from numerous regions. The northeastern U.S. (NEUS; Benz *et al.*, 1997), central U.S. (CUS; Erickson *et al.*, 2004), Tibet (McNamara *et al.*, 1996), Puerto Rico (PRSN; Motazedian and Atkinson, 2005), south-central Alaska (McNamara, 2000), Basin and Range (BRP; Benz *et al.*, 1997), and southern California (SoCal, Erickson *et al.*, 2004).

and tsunami monitoring (McNamara *et al.*, 2009). This is a first contribution on the understanding of attenuation parameters in the Haiti–Hispaniola region. Additional work such as detailed microzonation, near surface velocity profiling for V_{S30}, and regional phase propagation modeling are required to further improve our understanding of the ground-motion characteristics of the Haiti–Hispaniola region.

Conclusions

In this study we find that *Lg* propagates well in an ocean environment where the oceanic crust is thickened at an active tectonic boundary and determined frequency-dependent $Q(f)$ for the Hispaniola region using direct *S* and *Lg* waves over five distinct passbands from 0.5–16 Hz. For the distance range 250–700 km, we estimate an average frequency-dependent $Q(f) = 224(\pm 27)f^{0.64(\pm 0.073)}$ using horizontal *Lg* components. We also determine a $Q(f) = 142(\pm 21)f^{0.71(\pm 0.11)}$ for direct *S* waves at local distances—≤100 km. $Q(f)$ computed in this study is consistent with that determined in other studies in the region and is expected for a tectonically active environment.

Data and Resources

The waveforms used in this study include both horizontal and vertical components of motion from crustal earthquakes recorded at local and regional distances. Events analyzed include the devastating **M** 7.0 Haiti earthquake of 12 January 2010 and the rich sequence of aftershocks (Fig. 1; Ⓔ see Table S1, available in the electronic supplement to this paper). All waveforms were visually inspected and restricted to well-recorded (**M** ≥ 2.5) crustal earthquakes (depth ≤ 15 km). Data used in this study were digitally recorded at regional broadband stations operated by the Puerto Rico Seismic Network (PRSN) (Clinton *et al.*, 2006; Pujols, 2008), the seismic network in the Dominican Republic, the USGS GSN (McNamara *et al.*, 2006), and the Canadian National Network. In addition, 10 portable stations were deployed shortly after the Haiti **M** 7.0 earthquake (Hough *et al.*, 2010) (Fig. 1; Ⓔ see Table S2, available in the electronic supplement to this paper). Earthquake locations and magnitudes used in this study were obtained from the USGS Preliminary Determination of Epicenters (PDE). All waveform data, from both portable and permanent seismic stations, used in this study are archived and available for download from the IRIS DMC. Analysis and mapping software used includes SAC (Goldstein and Snoke, 2005), GMT (Wessel and Smith, 1991), and MATLAB.

Acknowledgments

The authors would like to thank Gari Mayberry, USGS-OFDA, for coordinating this international effort. We are indebted to Austin Volny of Haiti-BME for local support and technical assistance. We would like to thank G. Hayes, J. Boatwright, and R. Briggs for helpful discussions. Thoughtful comments were provided by V. Tsai, M. Petersen, Bill Walter and one anonymous BSSA reviewer.

References

Aki, K. (1980). Scattering and attenuation of shear waves in the lithosphere, *J. Geophys. Res.* **85,** 6496–6504, doi 10.1029/JB085iB11p06496.

Atkinson, G. M. (2004). Empirical attenuation of ground motion spectral amplitudes in southeastern Canada and the northeastern United States, *Bull. Seismol. Soc. Am.* **94,** 1079–1095.

Atkinson, G. M., and D. M. Boore (1995). Ground-motion relations for eastern North America, *Bull. Seismol. Soc. Am.* **85,** 17–30.

Atkinson, G., and R. Mereu (1992). The shape of ground motion attenuation curves in southeastern Canada, *Bull. Seismol. Soc. Am.* **82,** 2014–2031.

Aster, R., B. Borchers, and W. Thurber (2002). *Parameter Estimation and Inverse Problems*, Elsevier, Amsterdam.

Benz, H., A. Frankel, and D. Boore (1997). Regional *Lg* attenuation for the continental United States, *Bull. Seismol. Soc. Am.* **87,** 606–619.

Bird, P. (2003). An updated digital model of plate boundaries, *Geochem., Geophys., Geosyst.* **4,** 52, doi 10.1029/2001GC000252.

Boore, D. M. (1983). Stochastic simulation of high-frequency ground motions based on seismological models of the radiated spectra, *Bull. Seismol. Soc. Am.* **73,** 1865–1894.

Calais, E., A. Freed, G. Mattioli, F. Amelung, S. Jónsson, P. Jansma, T. Dixon Sang-Hoon Hong, C. Pfepetit, and R. Momplaisir (2010). Transpressional rupture of an unmapped fault during the 2010 Haiti earthquake, *Nat. Geosci.* **3,** 794–799, doi 10.1038/ngeo992.

Chavez, D., and K. Priestly (1986). Measurement of frequency dependent *Lg* attenuation in the Great Basin, *Geophys. Res. Lett.* **13,** 551–554, doi 10.1029/GL013i006p00551.

Clinton, J. F., G. Cua, V. Huérfano, C. von Hillebrandt-Andrade, and J. Martínez-Cruzado (2006). The current state of seismic monitoring in Puerto Rico, *Seismol. Res. Lett.* **77,** no. 5, 532–543, doi 10.1785/gssrl.77.5.532.

Crotwell, H. P., and T. J. Owens (2005). Automated receiver function processing, *Seismol. Res. Lett.* **76,** no. 6, 702–709, doi 10.1785/gssrl.76.6.702.

Dobrin, M. B., and C. H. Savit (1988). *Introduction to Geophysical Prospecting*, Fourth Ed., McGraw-Hill, New York, 867 pp.

Efron, B., and R. J. Tibshirani (1993). *An introduction to the bootstrap*, in Monographs on Statistics and Applied Probability, Chapman and Hall/CRC, London, 57 pp.

Erickson, D., D. E. McNamara, and H. M. Benz (2004). Frequency dependent *Lg Q* within the continental United States, *Bull. Seismol. Soc. Am.* **94,** no. 5, 1630–1643, doi 10.1785/012003218.

Frankel, A. (1991). Mechanisms of seismic attenuation in the crust: Scattering and anelasticity in New York state, South Africa and, southern California, *J. Geophys. Res.* **96,** 6269–6289.

Frankel, A., S. Harmsen, C. Mueller, E. Calais, and J. Haase (2010). Documentation for initial seismic hazard maps for Haiti, *USGS Open-File Report 2010-1067*, 12 pp.

Frankel, A., A. McGarr, J. Bicknell, J. Mori, L. Seeber, and E. Cranswick (1990). Attenuation of high-frequency shear waves in the crust: Measurements from New York state, South Africa and, southern California, *J. Geophys. Res.* **95,** 17,441–17,457.

Frankel, A. D., C. S. Mueller, T. P. Barnhardt, E. V. Lyendecker, R. L. Wesson, S. C. Harmsen, F. W. Klein, D. M. Perkins, N. C. Dickman, S. L. Hanson, and M. G. Hopper (2000). USGS national seismic hazard maps, *Earthq. Spectra* **16,** 1–19, doi 10.1193/1.1586079.

Frankel, A. D., M. D. Petersen, C. S. Mueller, K. M. Haller, R. L. Wheeler, E. V. Leyendecker, R. L. Wesson, S. C. Harmsen, C. H. Cramer, D. M. Perkins, and K. S. Rukstales (2002). Documentation for the 2002 update of the national seismic hazard maps, *USGS Open-file report 02-420*, 33 pp.

Goldstein, P., and A. Snoke (2005). SAC availability for the IRIS community, *DMS Electronic Newsletter* **7,** no. 1: available at http://www.iris.edu/news/newsletter/vol7no1/page1.htm (last accessed January 2012).

Gregersen, S. (1984). *Lg* wave propagation and crustal structure differences near Denmark and the North Sea, *Geophys. J. Int.* **79,** 217–234, doi 10.1111/j.1365-246X.1984.tb02852.x.

Gutenberg, B. (1955). Channel waves in the Earth's crust, *Geophysics* **20,** 283–294, doi 10.1190/1.1438141.

Hayes, G. P., R. W. Briggs, A. Sladen, E. J. Fielding, C. Prentice, K. Hudnut, P. Mann, F. W. Taylor, A. J. Crone, R. Gold, T. Ito, and M. Simons (2010). Complex rupture during the 12 January 2010 Haiti earthquake, *Nat. Geosci.* **3,** 800–805, doi 10.1038/ngeo977.

Hornbach, M. J., N. Braudy, R. W. Briggs, M. Cormier, M. B. Davis, J. B. Diebold, N. Dieudonne, R. Douilly, C. Frohlich, S. P. S. Gulick, H. E. Johnson III, P. Mann, C. McHugh, K. Ryan-Mishkin, C. S. Prentice, L. Seeber, C. C. Sorlien, M. S. Steckler, S. J. Symithe, F. W. Taylor, and J. Templeton (2010). High tsunami frequency as a result of combined strike-slip faulting and coastal landslides, *Nat. Geosci.* **3,** 783–788, doi 10.1038/ngeo975.

Hough, S. E., and J. G. Anderson (1988). High-frequency spectra observed at Anza, California: Implications for *Q* structure, *Bull. Seismol. Soc. Am.* **78,** 692–707.

Hough, S. E., J. R. Altidor, D. Anglade, D. Given, M. Guillard Janvier, J. Z. Maharrey, M. Meremonte, B. Saint-Louis Mildor, C. Prepetit, and A. Yong (2010). Localized damage caused by topographic amplification during the 12 January 2010 *M* 7.0 Haiti earthquake, *Nat. Geosci.* **3,** 778–782, doi 10.1038/ngeo988.

Isacks, B. L., and C. Stephens (1975). Conversion of *Sn* to *Lg* at a continental margin, *Bull. Seismol. Soc. Am.* **65,** 235–244.

Joshi, A., and S. Midorikawa (2004). A simplified method for simulation of strong ground motion using finite rupture model of the earthquake source, *J. Seismol.* **8,** 467–484, doi 10.1007/s10950-004-1595-z.

Kennett, B. (1986).*Lg* waves and structural boundaries, *Bull. Seismol. Soc. Am.* **76,** 1133–1141.

Knopoff, L., F. Schwab, and E. Kaussel (1973). Interpretation of *Lg*, *Geophys. J. Int.* **33,** 389–404, doi 10.1111/j.1365-246X.1973.tb02375.x.

Manaker, D. M., E. Calais, A. M. Freed, S. T. Ali, P. Przybylski, G. Mattioli, P. Jansma, C. Prepetit, and J. B. De Chabalier (2008). Interseismic plate coupling and strain partitioning in the northeastern Caribbean, *Geophys. J. Int.* **174,** 889–903, doi 10.1111/j.1365-246X.2008.03819.x.

Mann, P., E. Calais, J.-C. Ruegg, C. DeMets, P. E. Jansma, and G. S. Mattioli (2002). Oblique collision in the northeastern Caribbean from GPS measurements and geological observations, *Tectonics* **21,** 26, doi 10.1029/2001TC001304.

McNamara, D. E. (2000). Frequency dependent *Lg* attenuation in south-central Alaska, Geophys. Res. Lett. **27,** 3949–3952, doi 10.1029/2000GL011732.

McNamara, D., and W. Walter (2001). Mapping crustal heterogeneity using *Lg* propagation efficiency throughout the Middle East, Mediterranean, southern Europe and northern Africa, *Pure Appl. Geophys.* **158,** 1165–1188, doi 10.1007/PL00001219.

McNamara, D., T. Owens, and W. Walter (1996). Propagation characteristics of *Lg* across the Tibetan Plateau, *Bull. Seismol. Soc. Am.* **86,** 457–469.

McNamara, D., J. McCarthy, and H. Benz (2006). Improving earthquake and tsunami warning for the Caribbean Sea, Gulf of Mexico and the Atlantic coast, *U.S. Geol. Surv. Fact Sheet 2006-3012*, 4 pp: available at http://pubs.usgs.gov/fs/2006/3012/ (last accessed January 2012).

McNamara, D. E., Christa von Hillebrandt-Andrade, P. Earle, and R. Buland (2009). Seismic capabilities of an international Caribbean tsunami warning system, *Seismol. Res. Lett.* **80,** no. 2, 344.

Menke, W. (1980). *Geophysical Data Analysis: Discrete Inverse Theory* Academic Press, San Diego, California.

Motazedian, D., and G. Atkinson (2005). Ground-motion relations for Puerto Rico, in *Active tectonics and seismic hazards of Puerto Rico, the Virgin Islands, and offshore areas*, P. Mann (Editor), Geol. Soc. Am. Special Paper 385, 61–80.

Oliver, J., and M. Ewing (1957). Higher mode surface waves and their bearing on the Earth's mantle, *Bull. Seismol. Soc. Am.* **47,** 187–204.

Ottemoller, L. (2002). *Lg* wave *Q* tomography in Central America, *Geophys. J. Int.* **150,** 295–302, doi 10.1046/j.1365-246X.2002.01715.x.

Pasyanos, M. E, W. R. Walter, and E. M. Matzel (2009). A simultaneous multiphase approach to determine *P*-wave and *S*-wave attenuation of the crust and upper mantle, *Bull. Seismol. Soc. Am.* **99,** 3314–3325, doi 10.1785/0120090061.

Petersen, M. D., A. D. Frankel, S. C. Harmsen, C. S. Mueller, K. M. Haller, R. L. Wheeler, R. L. Wesson, Y. Zeng, O. S. Boyd, D. M. Perkins, N. Luco, E. H. Field, C. J. Wills, and K. S. Rukstales (2008). Documentation for the 2008 update of the United States national seismic hazard maps, *USGS Open-File Report 2008-1128*, 60 pp.

Prentice, C. S., P. Mann, A. J. Crone, R. D. Gold, K. W. Hudnut, R. W. Briggs, R. D. Koehler, and P. Jean (2010). Seismic hazard of the Enriquillo–Plantain Garden fault in Haiti inferred from palaeoseismology, *Nat. Geosci.* **3,** 789–793, doi 10.1038/ngeo991.

Press, F., and M. Ewing (1952). Two slow surface waves across North America, *Bull. Seismol. Soc. Am.* **42,** 219–228.

Raoof, M., R. B. Herrmann, and L. Malagnini (1999). Attenuation and excitation of three-component ground motion in southern California, *Bull. Seismol. Soc. Am.* **89,** 888–902.

Pujols, R. (2008). Seismic background noise of Puerto Rico, *Master's Thesis*, University of Puerto Rico, Mayaguez.

Tarr, A. C., S. Rhea, G. Hayes, A. Villaseñor, K. P. urlong, and H. Benz (2010). Seismicity of the earth 1900–2007, Caribbean plate and vicinity, *U.S. Geol. Surv. Open-File Rept. 2010-1083-A*, scale: 1:8,000,000; available at http://pubs.usgs.gov/of/2010/1083/a/.

Wessel, P., and W. Smith (1991). Free software helps display data, *Eos Trans. AGU* **72,** 445–446, doi 10.1029/90EO00319.

Xie, J., and B. J. Mitchell (1993). *Lg* coda *Q* across Eurasia, in *Yield and Discrimination Studies in Stable Continental Regions*, Mitchell, B. J. (Editor), Report PLTR- 91-2286, Phillips Laboratory, Hanscom Air Force Base, MA,77–91.

Zhang, T., and T. Lay (1995). Why the *Lg* phase does not traverse oceanic crust, *Bull. Seismol. Soc. Am.* **85,** 1665–1678.

Zeng, Y., J. G. Anderson, and F. Su (1994). A composite source model for computing realistic synthetic strong ground motions, *Geophys. Res. Lett.* **21,** 725–728, doi 10.1029/94GL00367.

Geological Hazards Science Center
U.S. Geological Survey
Golden, Colorado
mcnamara@usgs.gov
meremonte@usgs.gov
maharrey@usgs.gov
benz@usgs.gov
(D.M., M.M., J.Z.M., H.B.)

Bureau des Mines et de l'Energie
Delmas 19, rue nina 14, Box 2174
Port au Prince, Haiti
(S-L. M., J.R.A., D.A.)

U.S. Geological Survey
Pasadena, California
(S.E.H., D.G.)

Albuquerque Seismological Laboratory
U.S. Geological Survey
Albuquerque, New Mexico
lgee@usgs.gov
(L.G.)

U.S. Geological Survey
Seattle, Washington
afrankel@usgs.gov
(A.F.)

Manuscript received 7 May 2011